



Photocatalytic Degradation Mechanism of the Visible-Light Responsive BiVO₄/TiO₂ Core–Shell Heterojunction Photocatalyst

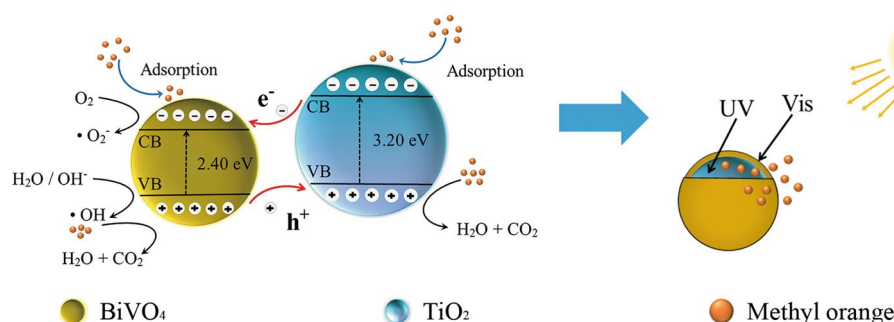
Kangkai Hu¹ · Lei E^{1,2} · Yajing Li³ · Xinyu Zhao¹ · Dan Zhao^{1,2} · Wei Zhao^{1,2} · Hui Rong¹

Received: 24 March 2019 / Accepted: 3 June 2019 / Published online: 6 June 2019
© Springer Science+Business Media, LLC, part of Springer Nature 2019

Abstract

The visible-light responsive BiVO₄/TiO₂ core–shell heterojunction photocatalyst was prepared by precipitation method. The crystal structure and optical properties of the samples were characterized. The XRD results indicated that the vector was anatase TiO₂. EDS, XPS and XRD showed that BiVO₄ was coated on the surface of TiO₂. SPV and UV–Vis spectra certified that the BiVO₄/TiO₂ photocatalyst possessed better absorption in the visible-light region (425–470 nm). The optical band gap of BiVO₄/TiO₂ photocatalyst ranged from 2.38 to 2.14 eV and decreased with the BiVO₄ amount increase from 2 to 6 mmol L⁻¹. Compared to TiO₂, the BiVO₄/TiO₂ photocatalyst exhibited much higher photocatalytic activity in degradation of methyl orange under visible light irradiation and lower photocatalytic activity in UV-light. Moreover, the effect of the different in formation mechanism of TiO₂/BiVO₄ and BiVO₄/TiO₂ on the photocatalytic activity was investigated in detail. The photocatalytic mechanism of BiVO₄/TiO₂ core–shell structure was discussed, which indicated that photoelectron reduction was the major degradation mechanism in this system. When TiO₂ particles were properly coated with BiVO₄ layer and the Bi/Ti molar ratio of 1:32, the composite photocatalyst could absorb UV-light and visible light at the same time, so the BiVO₄/TiO₂ core–shell heterojunction photocatalyst had the optimal photocatalytic activity in visible light irradiation, which was attributed to the spatial transfer of visible-excited high-energy electrons from TiO₂ to BiVO₄.

Graphical Abstract



Keywords BiVO₄/TiO₂ · Core–shell structure · Precipitation method · Photocatalytic mechanism · Energy level

Electronic supplementary material The online version of this article (<https://doi.org/10.1007/s10904-019-01217-w>) contains supplementary material, which is available to authorized users.

✉ Lei E
early@tcu.edu.cn

Extended author information available on the last page of the article

1 Introduction

With the development of scientific research, photocatalytic technology is widely used in environmental pollution and organic degradation [1–3]. Traditional large energy gap photocatalyst such as TiO₂ [4–6], ZnO [7, 8] and WO₃ [9, 10] cannot meet the requirements of the practical application. The modification of traditional photocatalyst and

development of new composite photocatalytic materials have attracted many researchers' attention [11–14]. BiVO_4 is an environment-friendly semiconductor material that has monoclinic scheelite crystal with a band gap width of 2.40 eV [15–17]. In addition, in view of the interaction between $\text{Bi}(6s)$ and $\text{O}(2p)$ orbitals at the top of the valence band, BiVO_4 behaves a strong response to visible-light [18, 19], which give rise to the excellent photocatalysis activity and has good properties of visible-light induced photochemical hydrolysis [20–23] and organic compound degradation [24–27]. Therefore, how to prepare new-type composite photocatalyst has become one of the research fields.

At present, there were two kinds of composite photocatalysts, $\text{TiO}_2/\text{BiVO}_4$ and $\text{BiVO}_4/\text{TiO}_2$, which are prepared by BiVO_4 and TiO_2 as vector respectively. TiO_2 is a sensitizer and BiVO_4 is a vector in $\text{TiO}_2/\text{BiVO}_4$ composite photocatalyst. On the contrary, BiVO_4 in $\text{BiVO}_4/\text{TiO}_2$ is a sensitizer and TiO_2 is a vector. A vector is a material that is loaded with certain trace substances/sensitizers to participate in chemical or physical processes. Xie et al. demonstrated that the photogenerated charge carriers in the $\text{TiO}_2/\text{BiVO}_4$ nanocomposite by hydrothermal method with a proper mole ratio (5%) displayed much longer lifetime and higher separation than those in the BiVO_4 alone [28]. Jung et al. reported the $\text{Si}/\text{TiO}_2/\text{BiVO}_4$ heterojunction films of photocurrents for solar water oxidation, herein, heterojunction photoanodes of Si and BiVO_4 could increase the efficiency of charge separation and reduce the onset potential of the photocurrent in a dual-absorber system [29]. Zhang et al. prepared the 3D $\text{FTO}/\text{TiO}_2/\text{BiVO}_4$ opal network photoanode with excellent photoelectrochemical performance by deposition method, which was owing to improving charge transport and separation efficiency [30]. Bian et al. researched that the exceptional photocatalytic activity of the 2D $\text{Au}/\text{TiO}_2/\text{BiVO}_4$ nanoflakes was comprehensively attributed to greatly enhanced charge separation, and the produced H atoms were dominant active radicals to initiate the conversion of CO_2 [31]. In addition, $\text{TiO}_2/\text{BiVO}_4$ nanowire heterostructure photoanodes [32] and $\text{TiO}_2\text{-BiVO}_4$ heterostructure in PEC biosensing [33] have been applied. Obregón et al. used the impregnation method to synthesize square rods and needle-like particles $\text{Er}^{3+}\text{-BiVO}_4/\text{TiO}_2$ ternary complexes, and the experiment results showed that the $\text{Er}^{3+}\text{-BiVO}_4/\text{TiO}_2$ materials had good photoactivity [34]. Hu et al. synthesized a wideband responsive $\text{BiVO}_4/\text{TiO}_2$ heterostructure material by sol-gel method, and the photodegradation results showed that the sample had good activity [35]. Zalfani et al. prepared novel 3DOM $\text{BiVO}_4/\text{TiO}_2$ nanocomposites by hydrothermal method, and the results showed that 3DOM $\text{BiVO}_4/\text{TiO}_2$ nanocomposites exhibited honeycomb-like shapes and possessed a highly prolonged lifetime of the photocatalysis degradation of RhB and increased separation of visible-light generated charges [36]. Wang et al. synthesized a novel

visible response $\text{BiVO}_4/\text{TiO}_2(\text{N}_2)$ nanotubes photoanode for photoelectrocatalytic applications, and the nitrogen-treated TiO_2 nanotube showed a high carrier concentration rate, thus resulting in a high efficient charge transportation and low electron-hole recombination rate in the $\text{TiO}_2\text{-BiVO}_4$ [37].

In the above reported studies, the $\text{TiO}_2/\text{BiVO}_4$ or $\text{BiVO}_4/\text{TiO}_2$ composite photocatalyst with special morphology can improve the efficiency of charge separation and has higher photocatalytic activity. However, owing to the complex photocatalytic process, it is very important to analyze the crystal structure and photocatalytic mechanism for improving the photocatalytic efficiency of $\text{BiVO}_4/\text{TiO}_2$. Besides, considering the fact that the morphological diversity of inorganic materials has a significant impact on functional diversification and potential application, there is still a huge potential for $\text{BiVO}_4/\text{TiO}_2$ composite to improve the photocatalytic activity by optimizing the preparation process to control the morphology, structure and surface properties. The synergistic effect between different components of nanoparticles in the core-shell structure can improve the photoelectrons mobility. Moreover, the sensitizer is covered on the surface of the vector in the core-shell structure, and the vector material is more stable. The two materials in the heterojunction structure have different energy band gaps, and the light-response range of the semiconductor can be broadened by adjusting the energy band gaps and the thickness of material layer. In this work, TiO_2 was used as a vector, with BiVO_4 layers on the surface act as a sensitizer to absorb photons and excite electron-hole pairs, and the visible-light responsive $\text{BiVO}_4/\text{TiO}_2$ core-shell heterojunction photocatalyst had been synthesized by precipitation method. The morphology, structure and photocatalytic properties of the photocatalyst were researched. Furthermore, the formation process of $\text{BiVO}_4/\text{TiO}_2$ core-shell heterojunction photocatalyst was deduced, and the different between the formation mechanism of $\text{TiO}_2/\text{BiVO}_4$ and $\text{BiVO}_4/\text{TiO}_2$ was discussed in detail. In further research, the photocatalytic mechanism of the $\text{BiVO}_4/\text{TiO}_2$ core-shell structure was discussed and band-edge potential positions were calculated. The research revealed that the photoelectron reduction was the main factor in the degradation of organic compounds by $\text{BiVO}_4/\text{TiO}_2$ photocatalyst.

2 Experimental

2.1 Material Preparation

The TiOSO_4 was commercial pure and other chemicals were analytical pure without further purification. In a typical procedure, a certain amount urea ($\text{CO}(\text{NH}_2)_2$) was added to 0.2 mol L^{-1} of TiOSO_4 solution with the $\text{Ti}:\text{NH}_3$ molar ratio of 1:2, which was stirred for 5 h under 95 °C to obtain

the precursor ($\text{TiO}(\text{OH})_2$), and TiO_2 was prepared by heat treatment of the precursor at $500\text{ }^\circ\text{C}$ for 2 h. Quantitative $\text{Bi}(\text{NO}_3)_3 \cdot 5\text{H}_2\text{O}$ and NH_4VO_3 were respectively dissolved into 30 mL deionized water to form two transparent solutions with agitation for 45 min. The above solutions were mixed together with the Bi:V molar ratio of 1:1. And then, an appropriate amount of TiO_2 powder was added to the mixed solution. The precursor of composite photocatalyst was obtained by adjusting pH to 7 with diluted ammonia solution ($\text{NH}_3 \cdot \text{H}_2\text{O}$) and was stirred continuously for 2 h under room temperature. The $\text{BiVO}_4/\text{TiO}_2$ core-shell heterojunction photocatalyst was synthesized with heat treatment of the reaction products at $400\text{ }^\circ\text{C}$ for 2 h. The sample is abbreviated as BT-X, and X represents the amount of BiVO_4 ($X\text{ mmol L}^{-1}$). The flow chart for preparing $\text{BiVO}_4/\text{TiO}_2$ photocatalyst was shown in Fig. 1.

2.2 Characterization

The micro morphology of the sample was observed by scanning electron microscope (SEM, JSM-7800F, Japan), and a large area energy dispersive spectrometer (EDS, X-Max^N, Britain) was used to analyze the composition of the sample. The optical absorption properties of the samples were conducted by the surface photovoltage spectroscopy (SPV, PL-SPS/IPCE 1000, China) in air ambient at room temperature with the wavelength range of 300–550 nm. The phase structure was characterized with X-ray diffraction (XRD, D/MAX-Ultima IV, Japan), with a source of $\text{Cu-K}\alpha$ radiation ($\lambda = 0.15406\text{ nm}$). Fourier transform infrared spectroscopy (FTIR, Thermo Nicole 380, America) was used to determine the changes of surface functional groups of the sample with the wavenumber range of $4000\text{--}400\text{ cm}^{-1}$. The surface

elements and their chemical states were characterized by X-ray photoelectron spectroscopy (XPS, ESCALAB 250Xi, America) with the energy analysis range of 0–1200 eV. The UV–Vis light absorption was studied by UV–Vis spectra (Cary 5000, America) in room temperature. The absorbance of methyl orange aqueous solution was measured with a UV–Vis spectrophotometer (UV-7230G, China) at the maximum absorption wavelength (505 nm) to determine the photocatalytic activity of the samples. The photoelectrochemical properties of the samples were tested by a three-electrode system of electrochemical workstation (CHI 760E, America).

2.3 Photocatalytic Experiment

The discoloration of the photocatalysis degradation of methyl orange (MO) was used to investigate the photocatalytic activity of the samples. The reaction temperature was maintained at room temperature. Typically, 0.1 g photocatalyst powders were placed in 25 mL MO (10 mg L^{-1} , pH 3) and the suspension was stirred in the dark for 1 h to ensure adsorption/desorption equilibrium before light on. After UV-light (30 W, $\lambda_{\text{max}} = 365\text{ nm}$) or visible-light (30 W, $\lambda > 420\text{ nm}$) was switched on, the absorbance of MO was measured at a given time intervals, with UV–Vis absorption spectra at maximum absorption wavelengths of 505 nm. Finally, the photocatalytic activity of the product was characterized by photocatalysis degradation (η) determined by using the following equation.

$$\eta = (1 - A_t/A_0) \times 100\%$$

where A_0 and A_t are the initial and final MO absorbance, respectively.

3 Results and Discussion

In order to determine whether anatase TiO_2 is suitable as a vector, we have studied its crystal structure first. The ball-stick model shows that the atoms are connected with each other by the Ti–O bond and arranged regularly to form a complete group of TiO_2 molecules (Fig. 2a₁), and the coordination number of Ti^{4+} ions is 6, forming TiO_6 octahedron and filling 50% of octahedral voids. The coordination number of O^{2-} ions is three, forming an OTi_3 plane delta group (Fig. 2b₁). From Fig. 2a₂ and b₂, we can see that O^{2-} is situated at the vertices of the unit cell to form a face-centered cubic packing with Ti^{4+} filling in body-centered of the octahedron and the space utilization rate is 74.05%. Anatase TiO_2 octahedron shows obvious skew square crystal distortion, and each octahedron is connected with around six octahedra in the form of four edge-shared and two corner-shared [38, 39]. It can be seen from Fig. 2c₁ that the coordination

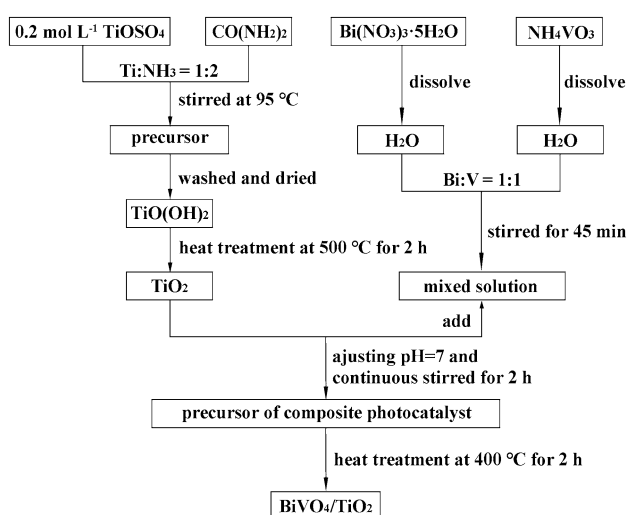


Fig. 1 The flow chart of preparation of $\text{BiVO}_4/\text{TiO}_2$ core-shell heterojunction photocatalyst

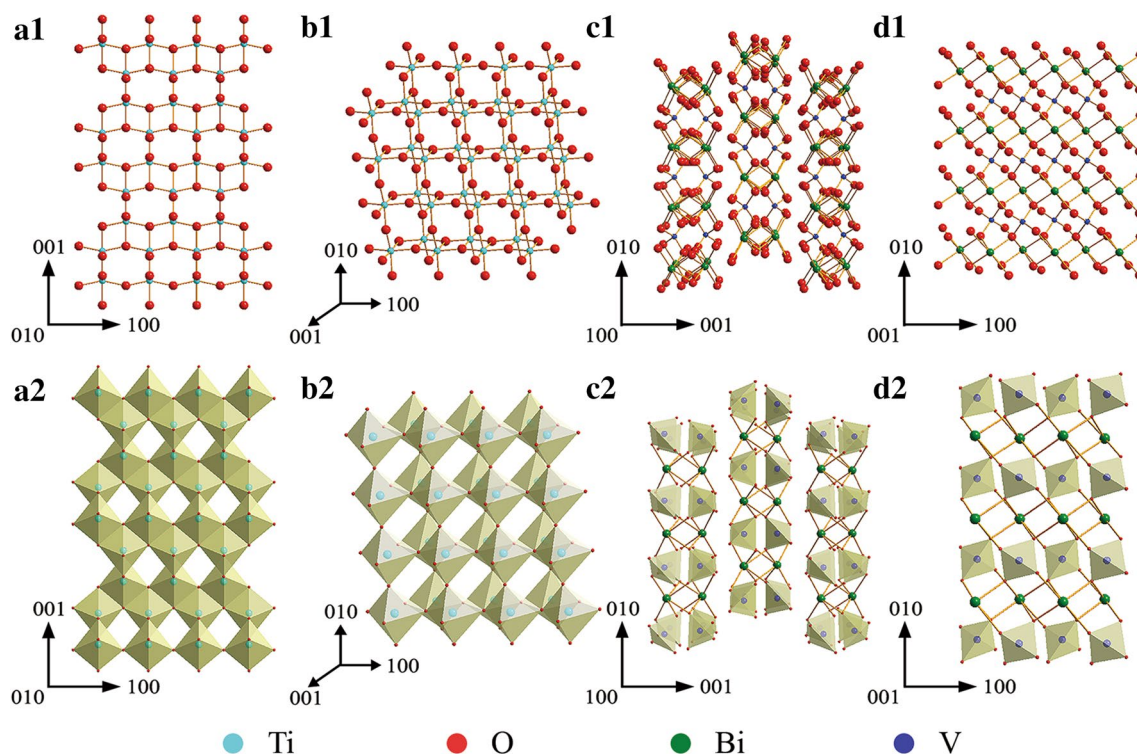


Fig. 2 Crystal structure of anatase TiO_2 and BiVO_4 . **a**₁, **b**₁ TiO_2 stick model; **a**₂, **b**₂ the chains of TiO_6 octahedron in TiO_2 ; **c**₁, **d**₁ BiVO_4 stick model; **c**₂, **d**₂ the chains of VO_4 tetrahedron in BiVO_4

number of Bi^{3+} , V^{5+} and O^{2-} in the BiVO_4 structure are 6, 4 and 2, forming BiO_6 oblique octahedron, VO_4 regular tetrahedron and OVBi_2 plane delta group. BiVO_4 forms unique molecular chains on the [010] direction (Fig. 2c₁), and the molecular chains aren't connected with each other. A complete structural chain is formed in the [001] direction, and the structural chain is connected regularly to form a stable crystal layer (Fig. 2d₁). Figure 2c₂ and d₂ shows that a polyhedron model is established with V element at the center of the crystal structure of BiVO_4 . The VO_4 group is tetrahedron as shown in Fig. 2c₂ and the Bi atom is connected with the around six tetrahedrons by Bi–O bond.

According to the research of Spek [40], in order to ensure the accuracy of the research results, it is necessary to establish and study the crystal structure of the product, and upon which subsequent research can be built. In photocatalytic system, the crystal structure is one of the factors that influence the carriers transport and photocatalytic activity in the photocatalytic process [41, 42]. As can be seen from the analysis of Fig. 2, the octahedra of TiO_2 crystal structure

are connected with each other to form a complete structural chain, which is more suitable as a vector. The crystal structure of the BiVO_4 forms molecular chains and it is easier to form a lamellar morphology. Therefore, BiVO_4 can be used as a sensitizer coated on the surface of TiO_2 to prepare $\text{BiVO}_4/\text{TiO}_2$ core–shell heterojunction photocatalyst.

Figure 3 shows two formation mechanisms of composite photocatalyst prepared from BiVO_4 and TiO_2 . The common composite photocatalyst is $\text{TiO}_2/\text{BiVO}_4$, and TiO_2 grows on the BiVO_4 layer surface as a sensitizer, which the formation process is shown in Fig. 3a. The photocatalytic activity of $\text{TiO}_2/\text{BiVO}_4$ nanocomposite is attributed to the unusual spatial transfer of visible-excited high-energy electrons from BiVO_4 to TiO_2 [28–33]. However, the photocatalyst prepared in this way is unstable and does not guarantee the uniform growth of TiO_2 on the BiVO_4 surface. So we prepared $\text{BiVO}_4/\text{TiO}_2$ core–shell heterojunction photocatalyst by using the method of Fig. 3b, with TiO_2 as a vector and BiVO_4 as a sensitizer. In the process of synthesis, BiVO_4 can grow on the TiO_2 surface more evenly and form stable core–shell structure photocatalyst.

Chemical equations for the preparation of TiO_2 .

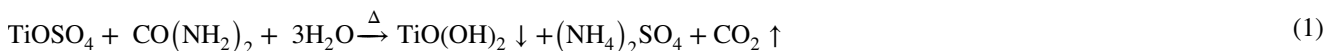
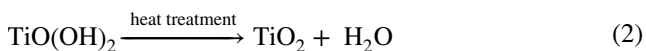
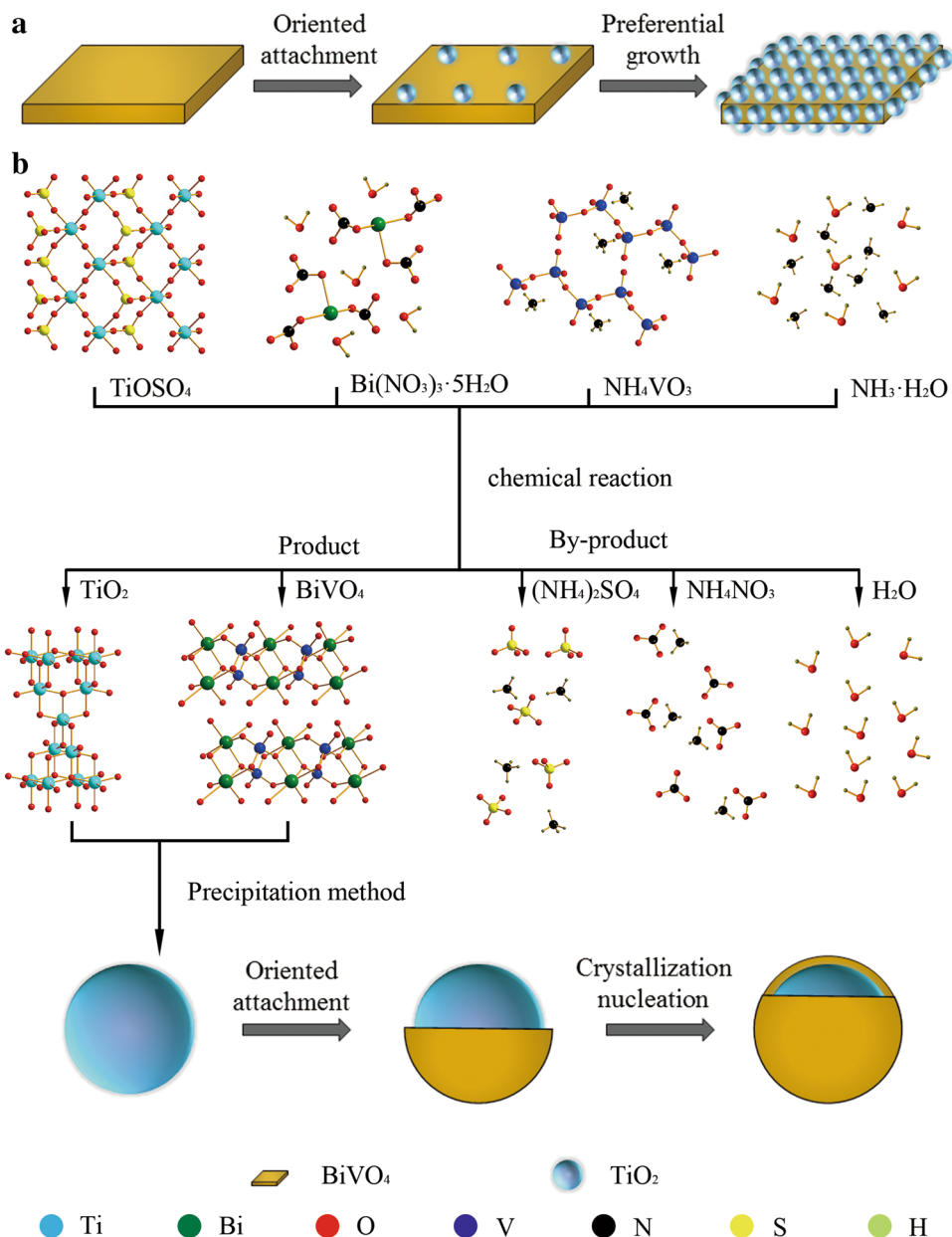
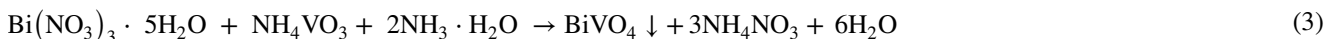


Fig. 3 Preparation scheme of the formation process of **a** $\text{TiO}_2/\text{BiVO}_4$ and **b** $\text{BiVO}_4/\text{TiO}_2$ photocatalysts



The chemical equation for the preparation of BiVO_4 is as follows.



It can be seen from Fig. 3b that the S–O–Ti bond of TiOSO_4 in solution breaks down to form TiO^{2+} , and TiO^{2+} combines with OH^- to form $\text{TiO}(\text{OH})_2$. During the heat-treatment of $\text{TiO}(\text{OH})_2$, the TiO_6 octahedrons are connected

with each other to form anatase TiO_2 structure. BiVO_4 formed by electrovalent bond of Bi^{3+} and VO_3^- ion group from NH_4VO_3 . The by-products of the synthesis process are common salts that do not cause environmental pollution during subsequent processing. The main products are TiO_2 and

BiVO_4 . The nucleation layer of BiVO_4 is crystallized and wrapped on the TiO_2 particles surface by the oriented attachment mechanism. It is worth noting that BiVO_4 does not fully encapsulate TiO_2 , and this incomplete encapsulation

Fig. 4 SEM of **a** TiO₂, **b** BT-2, **c** BT-4 and **d** BT-6

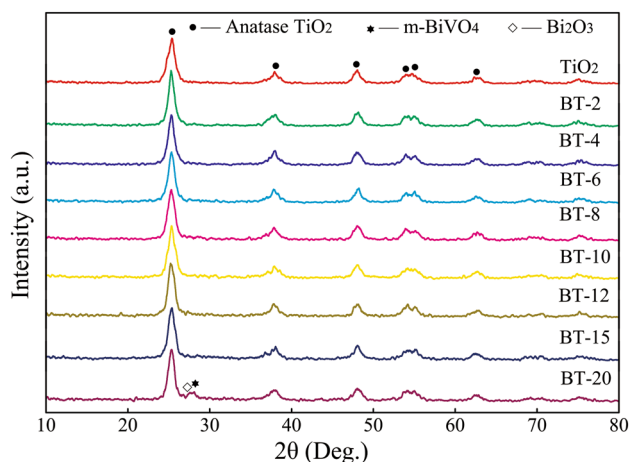
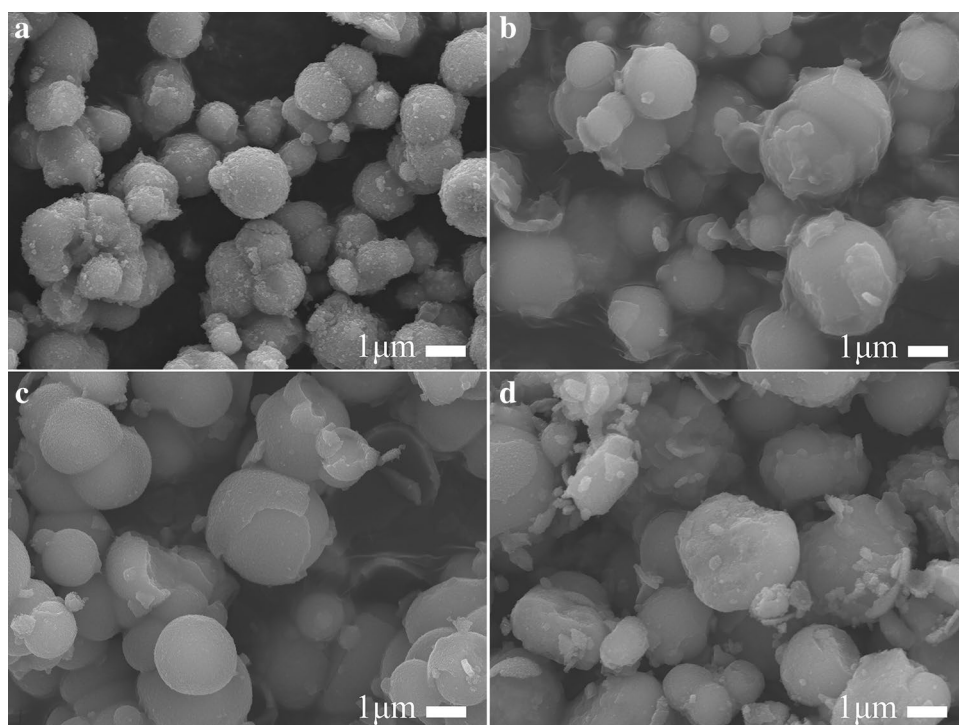


Fig. 5 XRD spectra of the samples

is one of the main factors affecting the BiVO₄/TiO₂ photocatalytic performance.

The morphology of TiO₂ particle is regularly spherical with rough surface, and the dispersion between the particles is good (Fig. 4a). BiVO₄/TiO₂ samples have smooth surface and layered structure, which indicates that BiVO₄ is formed on the surface of TiO₂. When the amount of BiVO₄ is increased from 2 to 6 mmol L⁻¹, the BiVO₄ layer is coated on the surface of TiO₂ and the exposed surface of TiO₂ is decreased (Fig. 4b–d). It can be observed that the

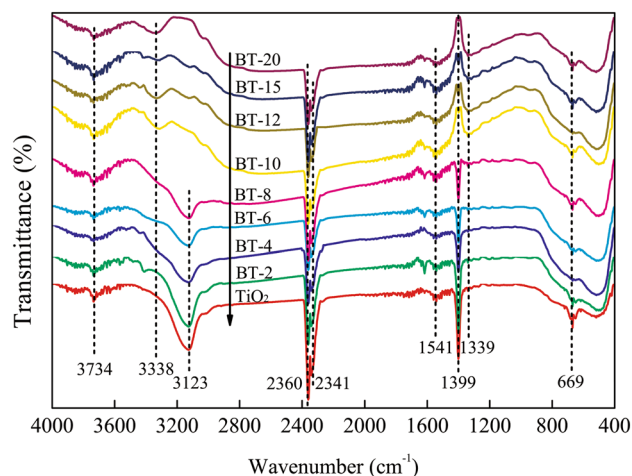


Fig. 6 FTIR spectra of the samples

particle size distribution of the sample is more uniform, and their average particle sizes are 1.07 μm, 1.65 μm, 1.72 μm and 2.05 μm (Fig. S1 of the Supporting Information). The average particle size of the BiVO₄/TiO₂ is raised with the increase of BiVO₄ amount. The surface composition of BT-2 is further studied and detected by EDS. The result indicated the presence of Bi, V and Ti elements at point A and B of the sample (Fig. S2 of the Supporting Information), and the ratio of Bi:V is about 2:3 and 1:2. So it can be speculated that BiVO₄ and other vanadium-containing oxides are formed.

The samples of BT-2 to BT-15 are anatase TiO_2 (JCPDS No. 21-1272), and no characteristic peaks of monoclinic or tetragonal BiVO_4 are found in the XRD pattern (Fig. 5). It may be considered that the amount of BiVO_4 incorporated is too small or the coating layer is too thin, so that the presence of BiVO_4 cannot be detected by XRD. However, BT-20 shows two weak intensity diffraction peaks of at 28.04° and 29.02° correspond to the (111) plane of Bi_2O_3 (JCPDS No. 27-0052) and the (-121) plane of monoclinic BiVO_4 (JCPDS No. 14-0688). This is consistent with the XRD spectrum of BiVO_4 (Fig. S3 of the Supporting Information), so it can be confirmed that the sample prepared by precipitation method is $\text{BiVO}_4/\text{TiO}_2$.

Figure 6 displays the FTIR spectra analysis for $\text{BiVO}_4/\text{TiO}_2$ and TiO_2 . The absorption peaks of all samples at range of around 3734 cm^{-1} , $2360\text{--}2341\text{ cm}^{-1}$, 1541 cm^{-1} and 1399 cm^{-1} are attributed to O–H stretching vibration. A weak peak at 3338 cm^{-1} possibly related to O–H stretching broad, and a peak of TiO_2 to BT-8 around 3123 cm^{-1} is attributed to OH groups. The O–H bonds and OH groups of the samples are mainly derived from adsorbed water. A prominent broad peak around 669 cm^{-1} is corresponding to Ti–O–Ti and Ti–O stretching vibration modes. It is noteworthy to mention that the additional peaks of the $\text{BiVO}_4/\text{TiO}_2$ samples in the range of 1339 cm^{-1} and 669 cm^{-1} correspond to Bi–O asymmetric vibration and Bi–O bending vibration. From the analysis results of the FTIR spectra, it is also confirmed that the sample prepared by the precipitation method is the $\text{BiVO}_4/\text{TiO}_2$ photocatalyst.

Figure 7 shows UV–Vis absorption spectra of $\text{BiVO}_4/\text{TiO}_2$ core–shell heterojunction photocatalyst. As illustrated, pure TiO_2 only presented absorbance in the UV-light region, with an absorption edge of 410 nm. While other samples exhibited better absorption in the UV-light and visible-light regions. It can be considered that the BiVO_4 layer caused

a red shift in absorption edge of the composite photocatalyst, but the absorption intensities of $\text{BiVO}_4/\text{TiO}_2$ is lower than pure TiO_2 in UV-light region. The efficient visible-light absorption abilities of the $\text{BiVO}_4/\text{TiO}_2$ ensured that it can generate sufficient electron–hole pairs under visible light irradiation. The optical band gap for the semiconductor photocatalyst was estimated using the following equation [43–45].

$$A h\nu = \alpha (h\nu - E_g)^{n/2}$$

where A is the absorption coefficient near the absorption edge; h is the Plank constant with the unit of eV; α is a constant; E_g is the absorption band gap energy; n depends on the characteristics of the transition in a semiconductor. BiVO_4 has a direct band gap, and n is 1 [45]. For TiO_2 , the value of n is 4 for the indirect transition [46]. The band gap of TiO_2 is found to be about 3.10 eV. As can be seen from Fig. 7, TiO_2 is an UV-light responsive catalyst material, and BiVO_4 is a visible light-responsive material. The $\text{BiVO}_4/\text{TiO}_2$ core–shell heterojunction photocatalyst prepared with TiO_2 as a vector is an UV-light responsive material. BiVO_4 as a sensitizer to reduce the band gap of the heterojunction and broaden its photoresponse range. Therefore, the BiVO_4 layer causes a red shift of the absorption edge of the composite photocatalyst, and causes the absorption intensities of $\text{BiVO}_4/\text{TiO}_2$ to be lower than pure TiO_2 in the UV light region. It is found that the band gap of $\text{BiVO}_4/\text{TiO}_2$ core–shell heterojunction photocatalyst ranged from 2.38 to 2.14 eV and decreased with the BiVO_4 amount increased from 2 to 6 mmol L^{-1} . BiVO_4 is a visible light-responsive material with a band gap about 2.37 eV. The BiVO_4 nanocrystals grow uniformly on the surface of TiO_2 to form a $\text{BiVO}_4/\text{TiO}_2$ core–shell heterojunction. The interfacial interaction between BiVO_4 and TiO_2 causes the band gap of $\text{BiVO}_4/\text{TiO}_2$ core–shell heterojunction decreased with the BiVO_4 amount increasing.

From Fig. 8a, it can be found that the surface of BT-6 is mainly composed of Ti, O, Bi, V and C elements, which C element comes from the inevitable oil pollution of XPS instrument. Four peaks $\text{Ti}^{3+} 2p_{3/2}$ at 457.9 eV, $\text{Ti}^{4+} 2p_{3/2}$ at 458.8 eV, $\text{Ti}^{3+} 2p_{1/2}$ at 463.4 eV and $\text{Ti}^{4+} 2p_{1/2}$ at 464.5 eV are obtained by fitting the Ti 2p binding energy of BT-6 (Fig. 8b). This indicates that Ti^{4+} exists in the $\text{BiVO}_4/\text{TiO}_2$ photocatalysts prepared by precipitation method. Fitting the O 1s binding energy obtained two peaks, where the peak at 529.8 eV corresponds to Ti–O binding energy and the peak at 530.8 eV corresponds to surface oxygen deficiency (O_v) binding energy (Fig. 8c). Two peaks are obtained by fitting Bi 4f binding energy of 159.3 eV corresponds to $\text{Bi} 4f_{7/2}$ and 164.7 eV corresponds to $\text{Bi} 4f_{5/2}$ (Fig. 8d). In Fig. 8e, there are three peaks of V 2p at 512.8 eV and 516.7 eV, which correspond to $\text{V} 2p_{3/2}$ and $\text{V} 2p_{1/2}$. There are three

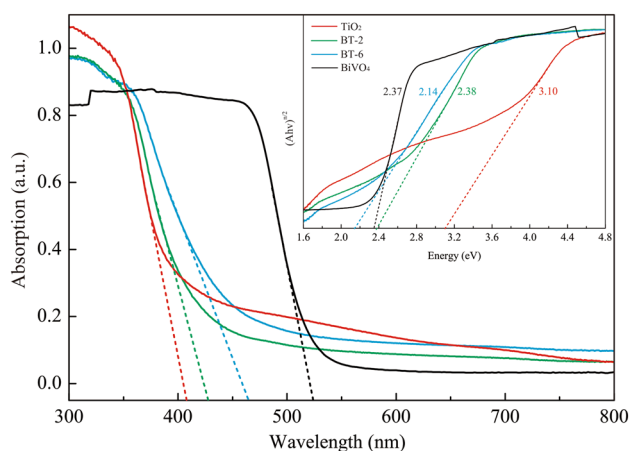


Fig. 7 UV–Vis absorption spectra of the samples, and inset graph shows the band gap energies

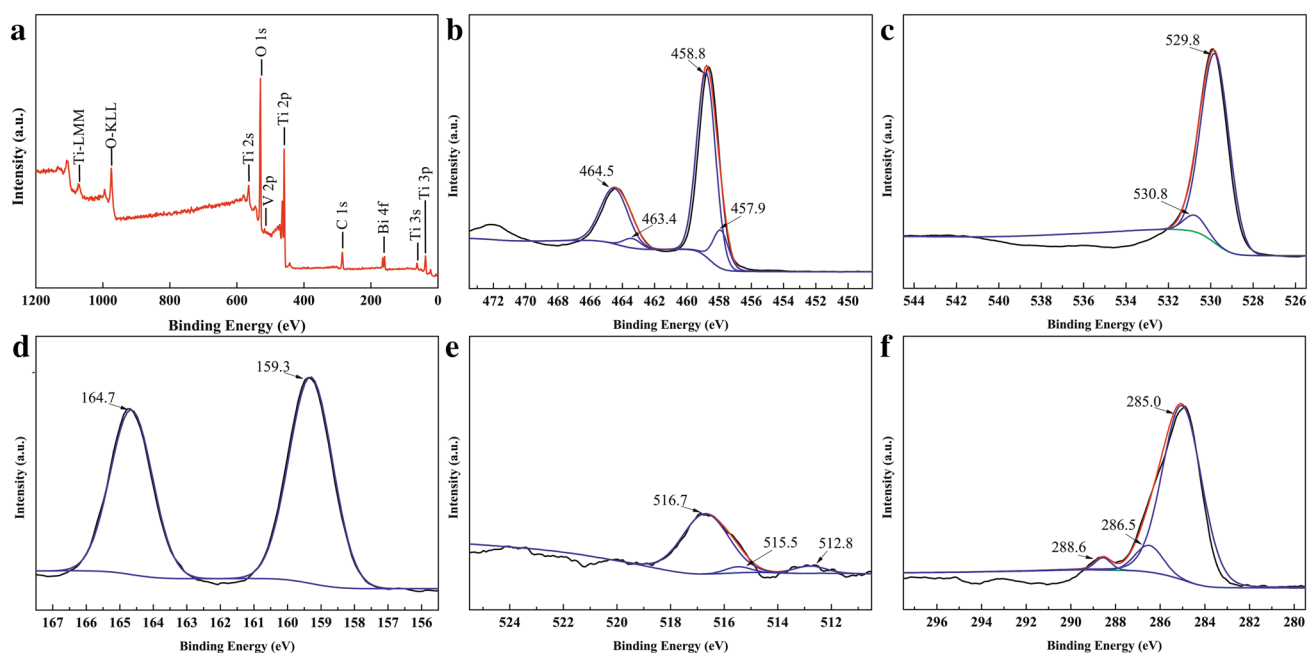


Fig. 8 The XPS **a** survey spectrum and the high-resolution spectra **b** Ti 2p, **c** O 1s, **d** Bi 4f, **e** V 2p and **f** C 1s of BT-6

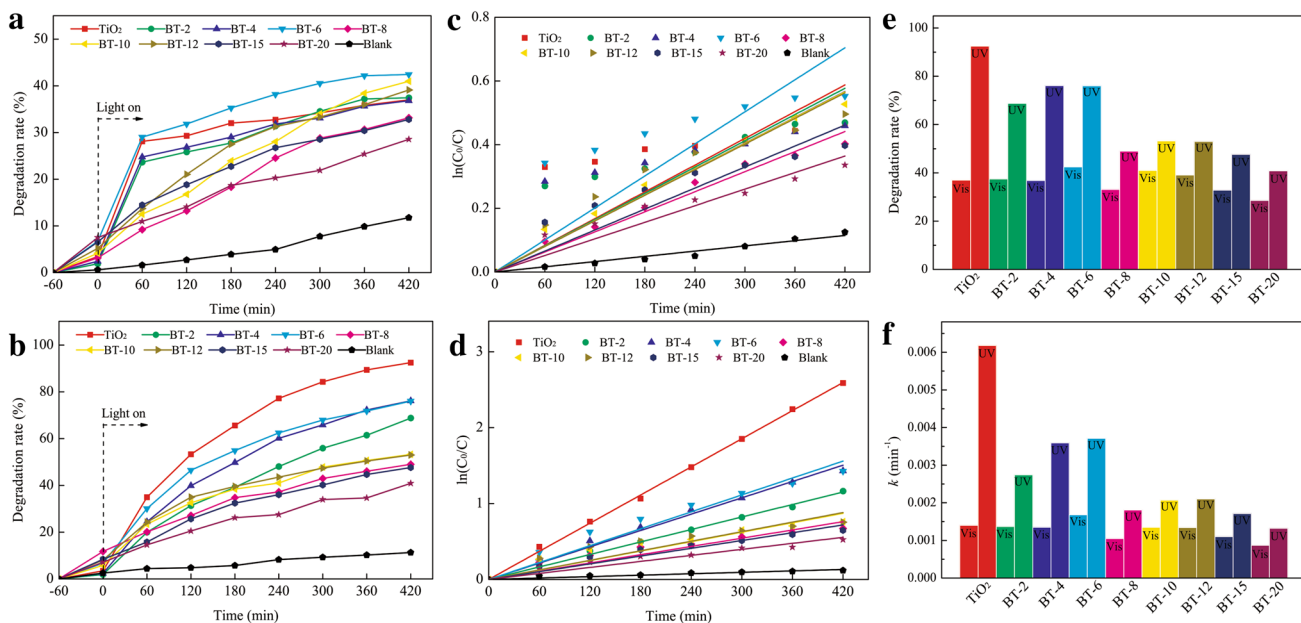


Fig. 9 Decolorization curve of MO degraded by samples under **a** visible light and **b** UV-light; plots of $\ln(C_0/C)$ versus irradiation time for MO representing the fit using a pseudo-first order reaction rate under

c visible light and **d** UV-light; **e** photodegradation rates and **f** pseudo-first order rate constants of the samples

peaks at 285.0 eV, 286.5 eV and 288.6 eV in C 1s, which are caused by oil pollution (Fig. 8f). XPS spectra show that BiVO_4 exists on the surface of BT-6 samples.

Figure 9 shows the photocatalytic activity of $\text{BiVO}_4/\text{TiO}_2$ core-shell heterojunction photocatalyst under visible light and UV-light. As the amount of BiVO_4 increases, the

photocatalytic activity of BT-2 to BT-12 under visible light irradiation is gradually increased, while the photocatalytic activity of BT-15 to BT-20 decreased (Fig. 9a). Among these samples, the photocatalytic activity of BT-6 is the best, and the decolorization rate of MO reached 42.43% after visible light irradiation for 7 h, which is 14.71% higher than that of

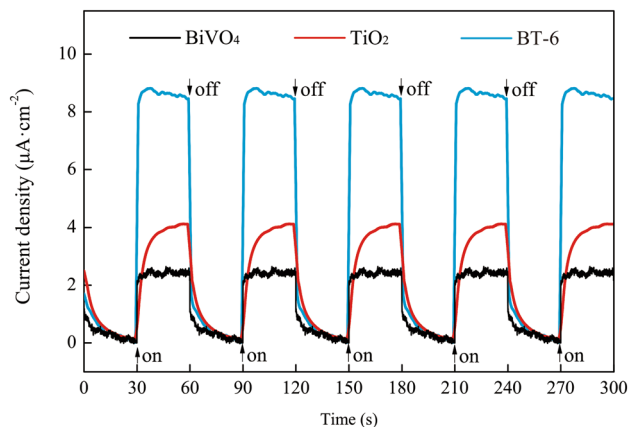
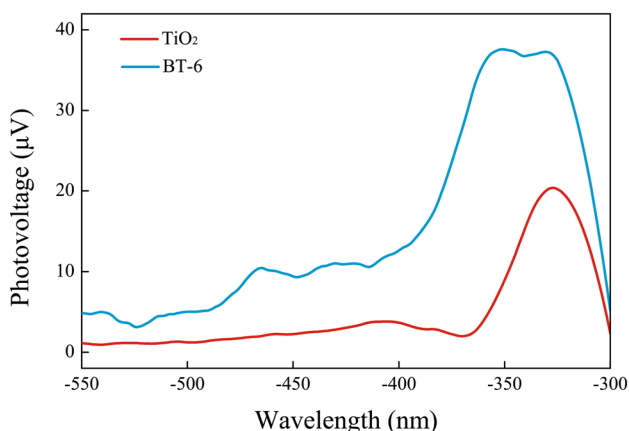
Table 1 Variation of refractive index (n) and extinction coefficient (ϵ) of TiO₂ and BiVO₄ as a function of wavelength [49, 50]

Semiconductors	300 nm		420 nm		600 nm	
	n	ϵ	n	ϵ	n	ϵ
TiO ₂	3.33	0.89	2.62	0	2.40	0
BiVO ₄	2.03	6.30	1.94	5.70	1.93	5.30

TiO₂ under the same conditions. Interestingly, the photocatalytic activity of BiVO₄/TiO₂ photocatalyst is lower than that of TiO₂ under UV-light irradiation (Fig. 9b). The photodegradation rates of BT-6 and TiO₂ reached 76.01% and 92.49% respectively after UV-light irradiation for 7 h. The kinetics of these photocatalytic reactions for low concentrations of MO were estimated from the linear plots of $\ln(C_0/C)$ against irradiation time, as displayed in Fig. 9c and d. Where C_0 is the MO concentration before irradiation, C is the MO concentration after irradiation [47]. The pseudo-first order rate constants (k , min⁻¹), determined from the slopes of $\ln(C_0/C)$ against irradiation time, are 0.00140 min⁻¹ for TiO₂ and 0.00168 min⁻¹ for BT-6 under visible light. In comparison, the apparent rate constants are 0.00618 min⁻¹ for TiO₂ and 0.00371 min⁻¹ for BT-6 under UV-light. The photocatalytic rate of BT-6 is 1.20 and 0.60 times of that of TiO₂ for degradation of MO under visible light and UV-light. It can be seen from Fig. 9e and f that BT-6 has the best photocatalytic activity and apparent rate under both UV-light and visible light irradiation. In conclusion, BiVO₄/TiO₂ core-shell heterojunction photocatalyst can improve the photocatalytic activity under visible light irradiation.

Owing to the light transmittance of BiVO₄ lower than TiO₂ [48], the refractive index (n) and extinction coefficient (ϵ) of TiO₂ and BiVO₄ decreased with wavelength increase from 300 to 600 nm [49, 50] (Table 1). When light illumination is on the surface of the material, the ability of incident light to refraction and reflection is proportional to the refractive index of the material. The extinction coefficients of TiO₂ and BiVO₄ at wavelength of 600 nm are 0 and 5.30 respectively. The extinction coefficient is larger, the amplitude attenuation of light irradiation on the surface of the sample is faster, and less light is entered the sample interior. Therefore, the morphology of BiVO₄ coated on the surface of TiO₂ will affect the response of its active site to UV-light. When the TiO₂ particles are completely coated with BiVO₄ layer, the TiO₂ particles cannot absorb the UV-light and become dead core, which resulted in the decrease of photocatalytic activity of BiVO₄/TiO₂ core-shell heterojunction photocatalysts. On the contrary, when the TiO₂ particles are partially coated with BiVO₄ layer, BiVO₄/TiO₂ can absorb both UV-light and visible light, so BiVO₄/TiO₂ core-shell heterojunction photocatalyst has the best photocatalytic activity. In this work, the molar ratio of Bi/Ti in BT-6 is 1:32.

In order to study the carrier separation ability of the BiVO₄/TiO₂ photocatalyst, the photocurrent density-time

**Fig. 10** Photocurrent density-time curves of the samples under illumination with 30 s light on/off cycles**Fig. 11** SPV spectra of TiO₂ and BT-6 measured in air

($I-t$) curve is characterized by a three-electrode electrochemical system using the experimental parameters as Ref. [39]. As shown in Fig. 10, when the light is turned on or off, the BT-6 photoelectrode has good photoresponse characteristics, which indicates that BiVO₄/TiO₂ core-shell heterojunction structure is beneficial to the separation and transport of carriers, and the photoresponse speed is fast. The photocurrent density of BT-6 is 8.73 $\mu\text{A cm}^{-2}$. The photocurrent density of the BiVO₄ and TiO₂ photoelectrode is 2.45 $\mu\text{A cm}^{-2}$ and 4.09 $\mu\text{A cm}^{-2}$, respectively. Compared with BiVO₄ and TiO₂ photoelectrode, the photocurrent density of BT-6 is increased by 256.33% and 113.45%.

SPV intensity can be used to evaluate the photocatalytic activity of semiconductor. From Fig. 11, we can find that the TiO_2 shows an obvious response in the UV-light region, and the weak SPV signal in the visible-light region. The BT-6 shows an obvious response in the UV-light and visible-light regions. The wavelength signals are negative for two samples, which indicates that the photoelectrons move preferentially toward the surface of TiO_2 and $\text{BiVO}_4/\text{TiO}_2$. The width and intensity of SPV response are different, which indicates that there are obvious differences in surface state density between TiO_2 and BT-6 photocatalysts. It is clear that the surface of TiO_2 has fewer photoelectrons, while the surface of BT-6 has more. This is due to the fact that the heterojunction structure of $\text{BiVO}_4/\text{TiO}_2$ is more favorable for the separation of photoelectrons and holes that can effectively form the surface space charge region. The built-in electric field is facilitated to separate of photoelectrons and holes, and the more positive photovoltage signals significantly promotes the more the surface net charge [51, 52].

Figure 12 is a schematic diagram of photo-induced carriers transport and degradation of MO by $\text{BiVO}_4/\text{TiO}_2$ core-shell heterojunction photocatalyst. Many studies have shown that the energy band gap is 2.40 eV of BiVO_4 and 3.20 eV of anatase TiO_2 , and the Fermi level is close to the conduction band. Hu et al. calculated the conduction/valence band position of anatase TiO_2 and BiVO_4 (Table 2) [35]. According to the energy level theory of semiconductors [53–55], the two materials must have the same Fermi level when the heterojunction structure is synthesized. In order to satisfy this condition, the energy level structures of BiVO_4 and TiO_2 are changes. The low band gap width of BiVO_4 electronic level will be reduced, and the high band gap width of TiO_2 electron energy level will be increased until the Fermi level reached the same energy value (Fig. 12a). The work function of BiVO_4 (5.27 eV) is

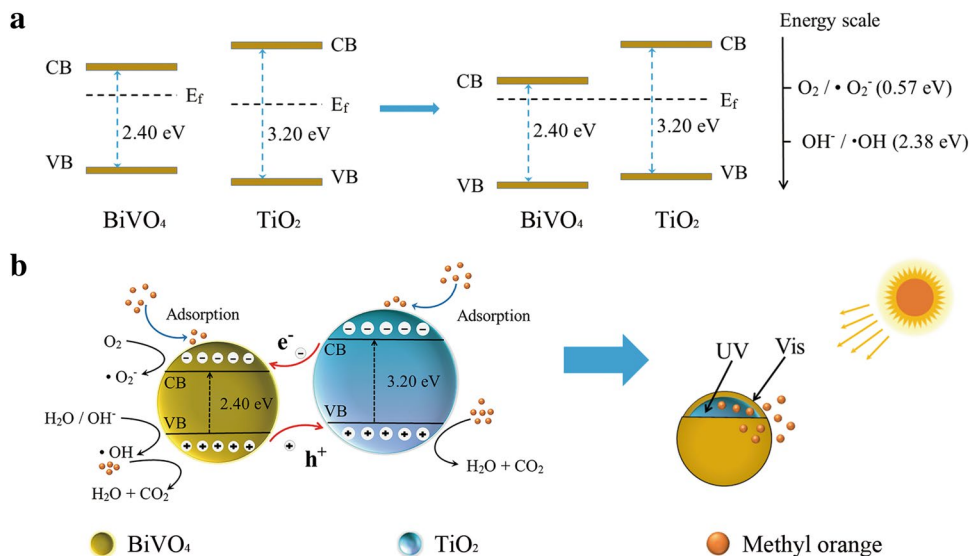
Table 2 Energy band gap, conduction band and valence band edge of TiO_2 and BiVO_4 [35]

Semiconductors	Conduction band edge (eV)	Valence band edge (eV)	Energy band gap (eV)
TiO_2	-0.20	3.00	3.20
BiVO_4	0.40	2.80	2.40

higher than that of TiO_2 (4.90 eV) [56, 57]. When the heterojunction is formed by BiVO_4 and TiO_2 , in order to match Fermi levels, the electrons transition from TiO_2 to the surface of BiVO_4 and form a space charge layer between BiVO_4 and TiO_2 . The surface of BiVO_4 is enriched in electrons, and holes are formed inside TiO_2 . A space charge layer is formed between TiO_2 and BiVO_4 . The semiconductor energy band bends upward to form a loss layer, and the Schottky barrier is formed on the interface of the heterojunction structure, which effectively suppresses the photoelectron-hole recombination and improves the photocatalytic activity of $\text{BiVO}_4/\text{TiO}_2$ [58].

The conduction band energy level of $\text{BiVO}_4/\text{TiO}_2$ core-shell heterojunction photocatalyst is less than the chemical potential of $\cdot\text{O}_2^-$ (0.57 eV), and this indicated that photoelectron (e^-) can reduce O_2 to $\cdot\text{O}_2^-$. The valence band edge of the $\text{BiVO}_4/\text{TiO}_2$ core-shell heterojunction photocatalyst is higher than the oxidation potential of $\cdot\text{OH}$ (2.38 eV), revealing that the photohole (h^+) is able to oxidize OH^- to yield $\cdot\text{OH}$ [59, 60]. When light source irradiates the $\text{BiVO}_4/\text{TiO}_2$ core-shell heterojunction photocatalyst, both TiO_2 and BiVO_4 absorb the illuminated light to generate electrons and holes from the respective energy level in a dual-light absorber system [29]. When the MO degraded by $\text{BiVO}_4/\text{TiO}_2$ core-shell heterojunction photocatalyst, photoelectrons transfer from the conduction band of the high energy level to

Fig. 12 Schematic illustration for **a** the energy band structure of the $\text{BiVO}_4/\text{TiO}_2$ heterojunction and **b** mechanism of photocatalytic degradation of MO by $\text{BiVO}_4/\text{TiO}_2$ photocatalyst



the low one, that is from TiO_2 to BiVO_4 surface. In contrast to the transmission of photoelectrons, photoholes transfer from the valence band of the low energy level to the high one, which from the BiVO_4 to the TiO_2 surface (Fig. 12b). However, the light transmittance of BiVO_4 is lower than TiO_2 . When MO adsorbed on the surface of $\text{BiVO}_4/\text{TiO}_2$ core-shell heterojunction photocatalyst, and only a few of MO can be degraded by electron reduction on the TiO_2 surface. Therefore, photo-induced carriers of $\text{BiVO}_4/\text{TiO}_2$ prepared in this study are mainly photoelectrons, which is consistent with the characterization of the SPV spectra.

In order to further determine the primary active species generated during the photocatalytic process over $\text{BiVO}_4/\text{TiO}_2$ core-shell heterojunction system, the capture agent of benzoquinone (BQ) and disodium edetate (EDTA-2Na) are used to capture superoxide ions (O_2^-) and holes (h^+), and the results are shown in Fig. 13. The adsorption of MO on the samples with BQ and EDTA-2Na increased significantly, and the photocatalytic rate of BQ ($k = 0.00161 \text{ min}^{-1}$) is higher than EDTA-2Na ($k = 0.00135 \text{ min}^{-1}$) and none ($k = 0.00135 \text{ min}^{-1}$). This result indicates that O_2^- plays a major role in the photocatalytic process of $\text{BiVO}_4/\text{TiO}_2$, and

O_2^- is derived from photoelectrons reduction O_2 . Therefore, photoelectron reduction is the main process of $\text{BiVO}_4/\text{TiO}_2$ photocatalysis, which is consistent with the results of SPV spectra and photocatalytic mechanism.

4 Conclusion

$\text{BiVO}_4/\text{TiO}_2$ core-shell heterojunction photocatalyst had been successfully prepared by precipitation method. Crystal structures analysis showed that TiO_2 was adapted as a vector and BiVO_4 as a sensitizer. UV-Vis spectra certified that the absorption of $\text{BiVO}_4/\text{TiO}_2$ photocatalyst increased in the visible region, and the optical band gap of $\text{BiVO}_4/\text{TiO}_2$ was 2.14–2.38 eV. According to the photocatalytic activity results, the decolorization rate of MO by $\text{BiVO}_4/\text{TiO}_2$ photocatalyst was 14.71% higher than that of TiO_2 after visible light irradiation for 7 h. However, the light transmittance was one of the main factors affecting the photocatalytic activity of $\text{BiVO}_4/\text{TiO}_2$ in UV-light irradiation. Thus, when BiVO_4 had an effective coverage area on the surface of TiO_2 particles, the $\text{BiVO}_4/\text{TiO}_2$ photocatalyst had excellent photocatalytic activity both in the UV-light and visible light irradiation. The photocatalytic mechanism and SPV spectra indicated that the separation of photo-induced carriers was facilitated under the $\text{BiVO}_4/\text{TiO}_2$ core-shell heterojunction structure, and the photoelectron reduction was the major degradation mechanism in this system.

Acknowledgements The authors gratefully acknowledge the financial support received from the Tianjin Natural Science Foundation (Grant No. 18JCYBJC87600) and the Key Projects of Tianjin Natural Science Foundation (Grant No. 16JCZDJC39100). The authors are indebted to Prof. L. Ge for his technical assistance in surface photovoltage spectroscopy (SPV).

Compliance with Ethical Standards

Conflict of interest The authors declare no competing financial interest.

References

1. R. Kaplan, B. Erjavec, G. Dražić, J. Grdadolnik, A. Pintar, Simple synthesis of anatase/rutile/brookite TiO_2 nanocomposite with superior mineralization potential for photocatalytic degradation of water pollutants. *Appl. Catal. B* **181**, 465–474 (2016). <https://doi.org/10.1016/j.apcatb.2015.08.027>
2. D. Zhang, G. Li, H. Wang, K.M. Chan, J.C. Yu, Biocompatible anatase single-crystal photocatalysts with tunable percentage of reactive facets. *Cryst. Growth Des.* **10**, 1130–1137 (2015). <https://doi.org/10.1021/cg900961k>
3. H. Li, L. Zhu, C. Ma, H. Zhang, TiO_2 hollow microspheres: synthesis, photocatalytic activity, and selectivity for a mixture of organic dyes. *Monatsh. Chem.* **145**, 29–37 (2014). <https://doi.org/10.1007/s00706-013-1012-9>

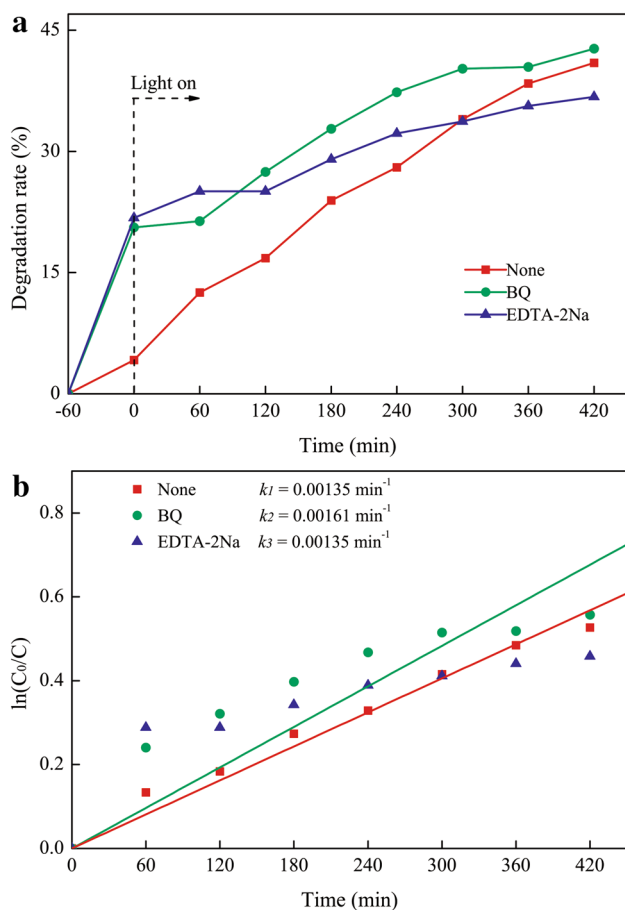



Fig. 13 **a** Decolorization curve of MO and **b** the fit using a pseudo-first order reaction rate by BT-10 under visible light

4. G. Li, H. Zhang, J. Lan, J. Li, Q. Chen, J. Liu, G. Jiang, Hierarchical hollow TiO₂ spheres: facile synthesis and improved visible-light photocatalytic activity. *Dalton Trans.* **42**, 8541–8544 (2013). <https://doi.org/10.1039/c3dt50503k>
5. P. Zhang, A. Li, J. Gong, Hollow spherical titanium dioxide nanoparticles for energy and environmental applications. *Particuology* **22**, 13–23 (2015). <https://doi.org/10.1016/j.partic.2015.03.001>
6. C. Zhang, Y. Zhou, Y. Zhang, S. Zhao, J. Fang, X. Sheng, T. Zhang, H. Zhang, Double-shelled TiO₂ hollow spheres assembled with TiO₂ nanosheets. *Chem. Eur. J.* **23**, 4336–4343 (2017). <https://doi.org/10.1002/chem.201602654>
7. M.A.M. Adnan, N.M. Julkapli, S.B.A. Hamid, Review on ZnO hybrid photocatalyst: impact on photocatalytic activities of water pollutant degradation. *Rev. Inorg. Chem.* **36**, 77–104 (2016). <https://doi.org/10.1515/revic-2015-0015>
8. C. Sushma, S.G. Kumar, Advancements in the zinc oxide nanomaterials for efficient photocatalysis. *Chem. Pap.* **71**, 2023–2042 (2017). <https://doi.org/10.1007/s11696-017-0217-5>
9. W.B. Cross, I.P. Parkin, Aerosol assisted chemical vapour deposition of tungsten oxide films from polyoxotungstate precursors: active photocatalysts. *Chem. Commun.* **14**, 1696–1697 (2003). <https://doi.org/10.1039/b303800a>
10. H. Zheng, J.Z. Ou, M.S. Strano, R.B. Kaner, A. Mitchell, K. Kalantar-zadeh, Nanostructured tungsten oxide-properties, synthesis, and applications. *Adv. Funct. Mater.* **21**, 2175–2196 (2011). <https://doi.org/10.1002/adfm.201002477>
11. M. Mohamed, W. Salleh, J. Jaafar, M. Rosmi, Z. Hir, M. Mutalib, A. Ismail, M. Tanemura, Carbon as amorphous shell and interstitial dopant in mesoporous rutile TiO₂: bio-template assisted sol-gel synthesis and photocatalytic activity. *Appl. Surf. Sci.* **393**, 46–59 (2017). <https://doi.org/10.1016/j.apsusc.2016.09.145>
12. M. Mohamed, J. Jaafar, M. Zain, L. Minggu, M. Kassim, M. Rosmi, N. Alias, N. Nor, W. Salleh, M. Othman, In-depth understanding of core-shell nanoarchitecture evolution of g-C₃N₄@C, N co-doped anatase/rutile: efficient charge separation and enhanced visible-light photocatalytic performance. *Appl. Surf. Sci.* **436**, 302–318 (2017). <https://doi.org/10.1016/j.apsusc.2017.11.229>
13. M. Mohamed, M. Zain, L. Minggu, M. Kassim, J. Jaafar, N. Amin, Y. Ng, Revealing the role of kapok fibre as bio-template for In-situ construction of C-doped g-C₃N₄@C, N co-doped TiO₂ core-shell heterojunction photocatalyst and its photocatalytic hydrogen production performance. *Appl. Surf. Sci.* **476**, 205–220 (2019). <https://doi.org/10.1016/j.apsusc.2019.01.080>
14. N. Rosman, W. Salleh, A. Ismail, J. Jaafar, Z. Harun, F. Aziz, M. Mohamed, B. Ohtani, M. Takashima, Photocatalytic degradation of phenol over visible light active ZnO/Ag₂CO₃/Ag₂O nanocomposites heterojunction. *J. Photochem. Photobiol. A* **364**, 602–612 (2018). <https://doi.org/10.1016/j.jphotochem.2018.06.029>
15. A. Kudo, K. Ueda, H. Kato, I. Mikami, Photocatalytic O₂ evolution under visible light irradiation on BiVO₄ in aqueous AgNO₃ solution. *Chem. Lett.* **53**, 229–230 (1998). <https://doi.org/10.1023/A:1019034728816>
16. M. Long, W. Cai, Photoelectrochemical properties of BiVO₄ film electrode in alkaline solution. *Chin. J. Catal.* **29**, 881–883 (2008). [https://doi.org/10.1016/S1872-2067\(08\)60069-8](https://doi.org/10.1016/S1872-2067(08)60069-8)
17. A.B. Murphy, P.R.F. Barnes, L.K. Randeniya, I.C. Plumb, I.E. Grey, M.D. Horne, J.A. Glasscock, Efficiency of solar water splitting using semiconductor electrodes. *Int. J. Hydrog. Energy* **31**, 1999–2017 (2006). <https://doi.org/10.1016/j.ijhydene.2006.01.014>
18. T. Saison, N. Chemin, C. Chaneac, O. Durupthy, V. Ruaux, L. Mariey, F. Mauge, P. Beaunier, J.P. Jolivet, Bi₂O₃, BiVO₄, and Bi₂WO₆: impact of surface properties on photocatalytic activity under visible light. *J. Phys. Chem. C* **115**, 5657–5666 (2011). <https://doi.org/10.1021/jp109134z>
19. L.S. Zhang, H.L. Wang, Z.G. Chen, P.K. Wong, J.S. Liu, Bi₂WO₆ micro/nano-structures: synthesis, modifications and visible-light-driven photocatalytic applications. *Appl. Catal. B* **106**, 1–13 (2011). <https://doi.org/10.1016/j.apcatb.2011.05.008>
20. T. George, S. Joseph, A.T. Sunny, S. Mathew, Visible-light photocatalytic activities of alpha-AgVO₃ nanorods and BiVO₄ nanobars. *Int. J. Nanotechnol.* **8**, 963–978 (2011). <https://doi.org/10.1504/IJNT.2011.044440>
21. A. Iwase, A. Kudo, Photoelectrochemical water splitting using visible-light-responsive BiVO₄ fine particles prepared in an aqueous acetic acid solution. *J. Mater. Chem.* **20**, 7536–7542 (2010). <https://doi.org/10.1039/c0jm00961j>
22. H. Kato, M. Hori, R. Kouta, Y. Shimodaira, A. Kudo, Construction of Z-scheme type heterogeneous photocatalysis systems for water splitting into H₂ and O₂ under visible light irradiation. *Chem. Lett.* **33**, 1348–1349 (2004). <https://doi.org/10.1246/cl.2004.1348>
23. Z.Q. Wang, W.J. Luo, S.C. Yan, J.Y. Feng, Z.Y. Zhao, Y.S. Zhu, Z.S. Li, Z.G. Zou, BiVO₄ nano-leaves: mild synthesis and improved photocatalytic activity for O₂ production under visible light irradiation. *CrystEngComm* **13**, 2500–2504 (2011). <https://doi.org/10.1039/C0CE00799D>
24. M. Long, W. Cai, J. Cai, B. Zhou, X. Chai, Y. Wu, Efficient photocatalytic degradation of phenol over Co₃O₄/BiVO₄ composite under visible light irradiation. *J. Phys. Chem. B* **38**, 20211–20216 (2007). <https://doi.org/10.1021/jp063441z>
25. S. Kohtani, M. Koshiko, A. Kudo, K. Tokumura, Y. Ishigaki, A. Toriba, K. Hayakawa, R. Nakagaki, Photodegradation of 4-alkylphenols using BiVO₄ photocatalyst under irradiation with visible light from a solar simulator. *Appl. Catal. B* **46**, 573–586 (2003). [https://doi.org/10.1016/S0926-3373\(03\)00320-5](https://doi.org/10.1016/S0926-3373(03)00320-5)
26. X. Zhang, Z.H. Ai, F.L. Jia, L.Z. Zhang, X.X. Fan, Z.G. Zou, Selective synthesis and visible-light photocatalytic activities of BiVO₄ with different crystalline phases. *Mater. Chem. Phys.* **103**, 162–167 (2007). <https://doi.org/10.1016/j.matchemphys.2007.02.008>
27. K. Soma, A. Iwase, A. Kudo, Enhanced activity of BiVO₄ powdered photocatalyst under visible light irradiation by preparing microwave-assisted aqueous solution methods. *Catal. Lett.* **144**, 1962–1967 (2014). <https://doi.org/10.1007/s10562-014-1361-y>
28. M. Xie, X. Fu, L. Jing, P. Luan, Y. Feng, H. Fu, Long-lived, visible-light-excited charge carriers of TiO₂/BiVO₄ nanocomposites and their unexpected photoactivity for water splitting. *Adv. Energy Mater.* **4**, 4–9 (2014). <https://doi.org/10.1002/aenm.201300995>
29. H. Jung, Y.C. Sang, C. Shin, B.K. Min, O.S. Joo, Y.J. Hwang, Effect of the Si/TiO₂/BiVO₄ heterojunction on the onset potential of photocurrents for solar water oxidation. *ACS Appl. Mater. Inter.* **7**, 5788–5796 (2015). <https://doi.org/10.1021/am5086484>
30. H. Zhang, C. Cheng, Three-dimensional FTO/TiO₂/BiVO₄ composite inverse opals photoanode with excellent photoelectrochemical performance. *ACS Energy Lett.* **2**, 813–821 (2017). <https://doi.org/10.1021/acsenrgylett.7b00060>
31. J. Bian, Y. Qu, X. Zhang, N. Sun, D. Tang, L. Jing, Dimension-matched plasmonic Au/TiO₂/BiVO₄ nanocomposites as efficient wide-visible-light photocatalysts to convert CO₂ and mechanism insights. *J. Mater. Chem. A* **6**, 11838–11845 (2018). <https://doi.org/10.1039/C8TA02889C>
32. J. Resasco, H. Zhang, N. Kornienko, N. Becknell, H. Lee, J. Guo, A.L. Briseno, P. Yang, TiO₂/BiVO₄ nanowire heterostructure photoanodes based on type II band alignment. *ACS Cent. Sci.* **2**, 80–88 (2016). <https://doi.org/10.1021/acscentsci.5b00402>
33. P.P. Liu, X. Liu, X.H. Huo, Y. Tang, J. Xu, H. Ju, TiO₂-BiVO₄ heterostructure to enhance photoelectrochemical efficiency for sensitive aptasensing. *ACS Appl. Mater. Interfaces.* **9**, 27185–27192 (2017). <https://doi.org/10.1021/acsami.7b07047>

34. S. Obregón, G. Colón, A ternary Er^{3+} - $\text{BiVO}_4/\text{TiO}_2$ complex heterostructure with excellent photocatalytic performance. *RSC Adv.* **4**, 6920–6926 (2014). <https://doi.org/10.1039/c3ra46603e>
35. Y. Hu, D. Li, Y. Zheng, W. Chen, Y. He, Y. Shao, X. Fu, G. Xiao, $\text{BiVO}_4/\text{TiO}_2$ nanocrystalline heterostructure: a wide spectrum responsive photocatalyst towards the highly efficient decomposition of gaseous benzene. *Appl. Catal. B* **104**, 30–36 (2011). <https://doi.org/10.1016/j.apcatb.2011.02.031>
36. M. Zalfani, B.V. Schueren, Z.Y. Hu, J.C. Rooke, R. Bourguiga, M. Wu, Y. Li, G.V. Tendeloo, B.L. Su, Novel 3DOM $\text{BiVO}_4/\text{TiO}_2$ nanocomposites for highly enhanced photocatalytic activity. *J. Mater. Chem. A* **3**, 21244–21256 (2015). <https://doi.org/10.1039/c5ta00783f>
37. R. Wang, J. Bai, Y. Li, Q. Zeng, J. Li, B. Zhou, $\text{BiVO}_4/\text{TiO}_2(\text{N}_2)$ nanotubes heterojunction photoanode for highly efficient photoelectrocatalytic applications. *Nano-Micro. Lett.* **9**, 14 (2017). <https://doi.org/10.1007/s40820-016-0115-3>
38. W.J. Yin, S. Chen, J.H. Yang, X.G. Gong, Y. Yan, S.H. Wei, Effective band gap narrowing of anatase TiO_2 by strain along a soft crystal direction. *Appl. Phys. Lett.* **96**, 221901 (2010). <https://doi.org/10.1063/1.3430005>
39. K. Hu, L. E, D. Zhao, C. Hu, J. Cui, L. Lai, Q. Xiong, Z. Liu, Hydrothermal synthesis of a rutile/anatase TiO_2 mixed crystal from potassium titanyl oxalate: crystal structure and formation mechanism. *CrystEngComm* **20**, 3363–3369 (2018). <https://doi.org/10.1039/c8ce00330k>
40. A.L. Spek, Single-crystal structure validation with the program PLATON. *J. Appl. Crystallogr.* **36**, 7–13 (2003). <https://doi.org/10.1107/S0021889802022112>
41. J. Tang, J. Ye, Correlation of crystal structures and electronic structures and photocatalytic properties of the W-containing oxides. *J. Mater. Chem.* **15**, 4246–4251 (2005). <https://doi.org/10.1039/b504818d>
42. P. Li, S. Ouyang, G. Xi, T. Kako, J. Ye, The effects of crystal structure and electronic structure on photocatalytic H_2 evolution and CO_2 reduction over two phases of perovskite-structured NaNbO_3 . *J. Phys. Chem. C* **116**, 7621–7628 (2012). <https://doi.org/10.1021/jp210106b>
43. X. Zhang, L. Zhang, T. Xie, D. Wang, Low-temperature synthesis and high visible-light-induced photocatalytic activity of BiOI/TiO_2 heterostructures. *J. Phys. Chem. C* **113**, 7371–7378 (2009). <https://doi.org/10.1021/jp900812d>
44. F. Wang, W. Li, S. Gu, H. Li, H. Zhou, X. Wu, Novel $\text{In}_2\text{S}_3/\text{ZnWO}_4$ heterojunction photocatalysts: facile synthesis and high-efficiency visible-light-driven photocatalytic activity. *RSC Adv.* **5**, 89940–89950 (2015). <https://doi.org/10.1039/c5ra16243b>
45. M. Wang, W. Li, Y. Zhao, S. Gu, F. Wang, H. Li, X. Liu, C. Ren, Synthesis of BiVO_4 - TiO_2 - BiVO_4 three-layer composite photocatalyst: effect of layered heterojunction structure on the enhancement of photocatalytic activity. *RSC Adv.* **6**, 75482–75490 (2016). <https://doi.org/10.1039/c6ra16796a>
46. K.L. Zhang, C.M. Liu, F.Q. Huang, C. Zheng, W.D. Wang, Study of the electronic structure and photocatalytic activity of the BiOCl photocatalyst. *Appl. Catal. B* **68**, 125–129 (2006). <https://doi.org/10.1016/j.apcatb.2006.08.002>
47. P. Dong, Y. Wang, B. Cao, S. Xin, L. Guo, J. Zhang, F. Li, Ag_3PO_4 /reduced graphite oxide sheets nanocomposites with highly enhanced visible light photocatalytic activity and stability. *Appl. Catal. B* **132**, 45–53 (2013). <https://doi.org/10.1016/j.apcatb.2012.11.022>
48. L. Hoffart, U. Heider, R.A. Huggins, W. Witschel, R. Jooss, A. Lentz, Crystal growth and conductivity investigations on BiVO_4 single crystals. *Ionics* **2**, 34–38 (1996). <https://doi.org/10.1007/BF02375866>
49. T. Siefke, S. Kroker, K. Pfeiffer, O. Puffky, K. Dietrich, D. Franta, I. Ohlidal, A. Szeghalmi, E.-B. Kley, A. Tünnermann, Materials pushing the application limits of wire grid polarizers further into the deep ultraviolet spectral range. *Adv. Opt. Mater.* **4**, 1780–1786 (2016). <https://doi.org/10.1002/adom.201600250>
50. S. Sarkar, N.S. Das, K.K. Chattopadhyay, Optical constants, dispersion energy parameters and dielectric properties of ultra-smooth nanocrystalline BiVO_4 thin films prepared by rf-magnetron sputtering. *Solid State Sci.* **33**, 58–66 (2014). <https://doi.org/10.1016/j.solidstatesciences.2014.04.008>
51. B. Wang, Z. Wan, H. Wu, S. Liu, Y. Chen, X. Sui, D. Yuan, Surface photovoltage: an efficient tool of evaluation of photocatalytic activity of materials. *Adv. Mater. Res.* **295–297**, 614–617 (2011). <https://doi.org/10.4028/www.scientific.net/AMR.295-297.614>
52. X. Qian, D. Qin, Q. Song, Y. Bai, T. Li, X. Tang, E. Wang, S. Dong, Surface photovoltage spectra and photoelectrochemical properties of semiconductor-sensitized nanostructured TiO_2 electrodes. *Thin Solid Films* **385**, 152–161 (2001). [https://doi.org/10.1016/S0040-6090\(01\)00771-4](https://doi.org/10.1016/S0040-6090(01)00771-4)
53. A.B. Anderson, Derivation of the extended Hückel method with corrections: one electron molecular orbital theory for energy level and structure determinations. *J. Chem. Phys.* **62**, 1187–1188 (1975). <https://doi.org/10.1063/1.430562>
54. F. Flores, J. Ortega, H. Vázquez, Modelling energy level alignment at organic interfaces and density functional theory. *Phys. Chem. Chem. Phys.* **11**, 8658–8675 (2009). <https://doi.org/10.1039/b902492c>
55. J. Ma, S.H. Wei, T.A. Gessert, K.K. Chin, Carrier density and compensation in semiconductors with multiple dopants and multiple transition energy levels: case of Cu impurities in CdTe. *Phys. Rev. B* **83**, 2335–2347 (2011). <https://doi.org/10.1103/PhysRevB.83.245207>
56. J.K. Cooper, S. Gul, F.M. Toma, L. Chen, P.A. Glans, J. Guo, J.W. Ager, J. Yano, I.D. Sharp, Electronic structure of monoclinic BiVO_4 . *Chem. Mater.* **26**, 5365–5373 (2014). <https://doi.org/10.1021/cm5025074>
57. G. Smith, R. Crook, J. Wadhawan, Measuring the work function of TiO_2 nanotubes using illuminated electrostatic force microscopy. *J. Phys.* **471**, 012045 (2013). <https://doi.org/10.1088/1742-6596/471/1/012045>
58. Y. Huang, J. Wu, Hydrogen production from water splitting by semiconductor oxides photocatalysis. *Prog. Chem.* **18**, 861–869 (2006). <https://doi.org/10.3321/j.issn:1005-281X.2006.07.003>
59. T. Saison, N. Chemin, C. Chanéac, O. Durupthy, L. Mariey, F. Maugé, V. Brezová, J.P. Jolivet, New insights into BiVO_4 properties as visible light photocatalyst. *J. Phys. Chem. C* **119**, 12967–12977 (2015). <https://doi.org/10.1021/acs.jpcc.5b01468>
60. P. Ju, Y. Wang, Y. Sun, D. Zhang, Controllable one-pot synthesis of a nest-like $\text{Bi}_2\text{WO}_6/\text{BiVO}_4$ composite with enhanced photocatalytic antifouling performance under visible light irradiation. *Dalton Trans.* **45**, 4588–4602 (2016). <https://doi.org/10.1039/c6dt00118a>

Publisher's Note Springer Nature remains neutral with regard to jurisdictional claims in published maps and institutional affiliations.

Affiliations

Kangkai Hu¹  · Lei E^{1,2}  · Yajing Li³ · Xinyu Zhao¹ · Dan Zhao^{1,2} · Wei Zhao^{1,2} · Hui Rong¹

Kangkai Hu
kanehu111@163.com

Yajing Li
yajingli@tcu.edu.cn

Xinyu Zhao
814457684@qq.com

Dan Zhao
zhaodan@tcu.edu.cn

Wei Zhao
zhaowei2004@tsinghua.org.cn

Hui Rong
hrong@tcu.edu.cn

¹ School of Materials Science and Engineering, Tianjin Chengjian University, Tianjin 300384, China

² Tianjin Key Laboratory of Building Green Functional Materials, Tianjin Chengjian University, Tianjin 300384, China

³ School of Environmental and Municipal Engineering, Tianjin Chengjian University, Tianjin 300384, China